CrossMark
←click for updates

Tribological characteristics of few-layer graphene over Ni grain and interface boundaries†

Manoj Tripathi,[a] Firas Awaja,[a] Guido Paolicelli,[b] Ruben Bartali,[a] Erica Iacob,[a] Sergio Valeri,[c] Seunghwa Ryu,[d] Stefano Signetti,[e] Giorgio Speranza[a] and Nicola Maria Pugno*[e,a,f]

The tribological properties of metal-supported few-layered graphene depend strongly on the grain topology of the metal substrate. Inhomogeneous distribution of graphene layers at such regions led to variable landscapes with distinguishable roughness. This discrepancy in morphology significantly affects the frictional and wetting characteristics of the FLG system. We discretely measured friction characteristics of FLG covering grains and interfacial grain boundaries of polycrystalline Ni metal substrate *via* an atomic force microscopy (AFM) probe. The friction coefficient of FLG covered at interfacial grain boundaries is found to be lower than that on grains in vacuum (at 10^{-5} Torr pressure) and similar results were obtained in air condition. Sliding history with AFM cantilever, static and dynamic pull-in and pull-off adhesion forces were addressed in the course of friction measurements to explain the role of the out-of-plane deformation of graphene layer(s). Finite element simulations showed good agreement with experiments and led to a rationalization of the observations. Thus, with interfacial grain boundaries the FLG tribology can be effectively tuned.

Freely suspended graphene is attractive in science due to its extraordinary properties.[1,2] However, its interaction with a substrate, like a metal, plays a vital role to fill the gap between science and technological applications, such as heterogeneous catalysts,[3] strengthening components,[4,5] transparent electrodes,[6] and NEMS/MEMS,[7,8] among others. Graphene can tune the water contact angle[9] and displays high mechanical

[a]*Centre for Materials and Microsystems, Fondazione Bruno Kessler, via Sommarive 18, I-38123, Povo (Trento), Italy*

[b]*CNR, Istituto Nanoscienze – Centro S3, Via Campi 213/a, I-41125 Modena, Italy*

[c]*Dipartimento di Scienze Fisiche Informatiche e Matematiche, Università di Modena e Reggio Emilia, via Campi 213/a, I-41125 Modena, Italy*

[d]*Department of Mechanical Engineering, Korea Advanced Institute of Science and Technology, Daejeon 34141, Korea*

[e]*Laboratory of Bio-Inspired and Graphene Nanomechanics, Department of Civil, Environmental and Mechanical Engineering, University of Trento, via Mesiano 77, I-38123 Trento, Italy*

[f]*School of Engineering and Materials Science, Queen Mary University of London, Mile End Road, E1 4NS London, UK. E-mail: nicola.pugno@unitn.it*

†Electronic supplementary information (ESI) available: Filtered derivative of raw topographic data to distinguish between flat and rough surfaces that correspond to grain and interfacial grain boundaries respectively. AFM intermittent contact mode showing high resolution topography interfacial boundary between two grains. Raman spectra of epitaxial graphene on polycrystalline Ni that include its grain and interfacial grain boundaries. The reference samples that include a single layer graphene epitaxial grown on Ni (111) and single layer graphene mechanically exfoliated and deposited on SiO_2 substrate. Raman spectroscopy map of epitaxial grown graphene and transferred to silica substrate. Scheme of the FEM model setup. See DOI: 10.1039/c5nr06273j

strength, stiffness, inertness and stability[10–12] which offer durable, rustproof and antiwear coatings.[13] At micro-nano tribocontacts, where a liquid state lubricant squeezes out under pressure condition,[14] graphene could be used as a very thin solid state lubricant.[15,16] Researchers have observed that graphene substantially reduces the friction force of the substrate on which it is deposited. Filleter *et al.*[17] measured a dynamic coefficient of friction (COF) of 0.004 and 0.001 for epitaxial-grown monolayer and bi-layer graphene respectively over SiC (0001) in UHV condition using a polycrystalline diamond-coated tip. The recorded friction forces resulted nearly 25 times lower than on a carbon-rich interface and nearly half those of graphite. Marsden *et al.*[18] obtained a COF of 0.12–0.18 for Chemical Vapor Deposited (CVD) Gr–Cu and 0.7 ± 0.2 for bare Cu substrate using a silica tip in air condition. Using a similar type of tip configuration, Egberts *et al.*[19] obtained a COF almost statistically indistinguishable from zero (-0.004 ± 0.009) for Gr–Cu compared to 0.57 ± 0.03 for bare copper substrate in air condition. Berman *et al.*[20] observed that CVD-grown few-layered graphene (FLG; about 6–7 layers) on Ni has lower friction with respect to silica substrate (ratio ~1/19) and to highly ordered pyrolytic graphite (HOPG, ratio ~1/2). Similar investigation has been carried out by Kim *et al.*[16] at both microscale and nanoscale, where they measured a COF of 0.03 between fused silica lens and CVD-grown Gr–Ni in air condition. They found a decrease in real contact area between the fused silica lens (as slider) and the

graphene. The stronger adhesion between graphene and underlying Ni substrate is responsible for such a low COF compared to graphene on other substrates (Cu and SiO_2). Additionally, the higher roughness of FLG on Ni also contributed by a decrease in real contact area between fused silica lens and graphene.

Graphene produced either from mechanical exfoliation[21] or from thermal decomposition[22] shows layers number- and substrate-dependent characteristics. Different mechanical responses have been observed for substrate-supported graphene under Friction Force Microscopy (FFM) operations at the nanoscale. In one case, graphene loosely adhered to substrate (like the Gr–SiO_2 system) interacted strongly with a sliding atomic force microscopy (AFM) tip due to relatively higher adhesion and locally buckled followed by out-of-plane deformation. This results in an increase in the contact area under the tip apex along the scanning direction, opposing to its motion and causing higher friction. This phenomenon is called "puckering"[21] that is enhanced in the case of exposed graphene (top graphite layer) in ambient air condition.[23] A theoretical follow-up attributed this behaviour to a non-destructive form of viscoelastic ploughing.[24] In another case, an increased resistance to out-of-plane deformation, and correspondingly, lower friction could be achieved through strong interaction with the substrate (such as on mica[25] and on Ni.[26,27]). Molecular dynamics (MD) simulations demonstrated that stacked graphene would be a better lubricant to reduce friction for an AFM tip than loose graphene.[24] Several reports suggested functionalized graphene (e.g. adsorption with fluoride ion, hydrogen) to raise out-of-plane bending stiffness. Chemically modified graphene with adsorption of a third body (like hydrogen and fluoride ions) enhances friction at the nanoscale between slider and substrate[28,29] even up to 4-fold in the case of fluorination.

There is still a limited understanding of the frictional characteristics of graphene and its behaviour over different substrates, especially for metallic supports. All of the results described above for metal-supported graphene did not include the influence of metal grains and grain boundaries. And our previous investigation revealed that a single layer of graphene grown on Ni (111) crystal shows lower friction force than graphite against a silica tip in vacuum.[30] Here, we are proposing new criteria that influence the tribology of graphene at the interfacial grain boundaries of the substrate. Ni is considered here as a case study. From a tribological perspective, graphene on polycrystalline Ni (Gr/Ni–P) is a composite system equivalent to graphite (HOPG) but with finite layers, possessing higher average roughness (nearly 70 times) due to the presence of interfacial grain boundaries and randomly oriented planes of Ni grains. Our current work is different from that reported in the literature at the microscale,[16] where friction measurement has accumulated results from grains and interfacial grain boundaries. We differentiated friction forces from grains and interfacial grain boundaries and resolved their contributions exclusively. In our present work, the series of investigations are as follows: in the first part, the morphology of Gr/Ni–P is discussed. In the second part, the morphological

influence over wettability is described. In the final section, we show the morphological influence over frictional characteristics of graphene in vacuum condition using graphene-covered grain domains and interfacial grain boundaries.

Results and discussion

Morphological description of bare polycrystalline Ni and CVD-grown graphene on polycrystalline Ni

Polycrystalline Ni metal contains surface features/regions that are randomly oriented, relative to each other, and are separated by thin boundary areas. We term those regions as "Ni grain" and "Ni interface boundary" (Ni-IB), respectively, throughout the paper. A typical example of a polycrystalline nickel metal substrate is presented in Fig. 1(a). This is a 3-D AFM image where Ni grains and Ni-IB are clearly visible. The average roughness R_a of a particular grain region (size 600 × 600 nm^2) is nearly 0.2 nm, while for the entire image area (2 × 2 μm^2 that includes several interface regions) R_a increases to about 0.3 nm. In Fig. 1(b), the friction force measured on the same Ni region is presented. The friction signal is higher at Ni-IB than on Ni grain due to the involvement of the extra atom at the edges felt by the tip apex[31]. During CVD operations these Ni-IBs are potential nucleation sites for multilayer graphene during segregation-growth mechanism.[32] Therefore, pronounced roughness is expected for the graphene-covered polycrystalline Ni (Gr/Ni–P) with abundant Ni-IB, since it facilitates the formation of multilayer graphene at Ni-IB due to higher availability of nucleation sites.

Fig. 1(c) represents a topographic image of a 5 × 5 μm^2 area of CVD-produced multilayer graphene on polycrystalline Ni substrate. Unlike polycrystalline metal, CVD-grown graphene produces an uneven distribution of graphene layers that cover both Ni grains and Ni interfacial grain boundaries. Nevertheless, there are some regions where graphene is relatively uniform and flat, referred to as "grains". The other regions that lie between two or more grain regions and comprise defects and steps are referred to as interface grain boundary[32] "IB". The measured average roughness R_a, over sampling regions of 500 × 500 nm^2, was 3.0 nm for grain zone and 5.9 nm for IB zone. Fig. 1(d) shows a friction force map (nN) obtained in parallel during the topography acquisition of Fig. 1(c). The map is obtained by subtracting the lateral force felt by the AFM probe moving in the trace direction from that in the re-trace direction, i.e. (trace-retrace)/2, that is a half of te so-called "trace minus retrace" (TMR). This standard procedure is used to minimize the topographical influence of the sample over the actual friction signals. It is observed that lateral force (F_L) is lower at graphene IB than at grain regions (Fig. 1(d)), in contrast to friction force observed at bare Ni metal, at Ni facet, and at grain boundary metal (Fig. 1(b)). Over all, Fig. 1 reveals that IB region may have higher accumulation of carbon layers that increases the roughness and might significantly influence the frictional characteristics of the whole composite. We will validate this observation in the following section.

Metal Ni-P

(a) **Topography** 9 nm

400 nm

0.00 nm

(b) **Friction force** 68.5 nN

400nm

0.00 nN

CVD Gr/Ni-P

(c) **Topography** 73 nm

990 nm

0.00 nm

(d) **Friction force** 60.0 nN

Grain region

IB region

990nm

0.00 nN
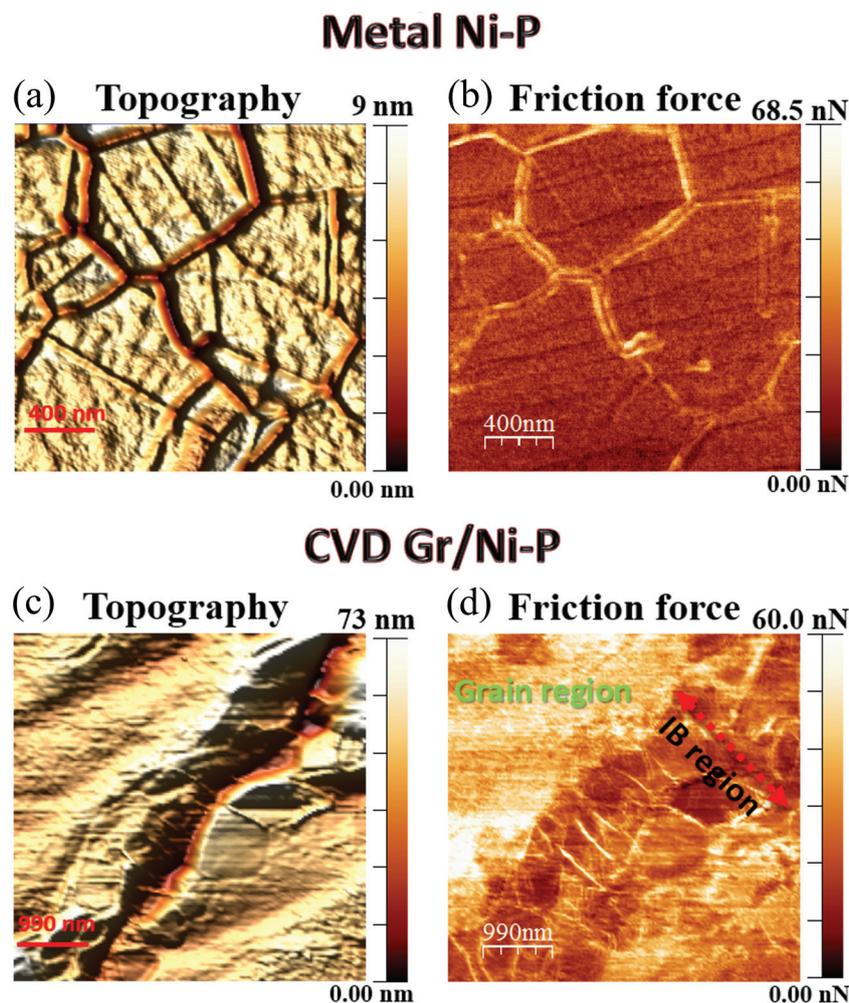
Fig. 1 Topography of polycrystalline bare and graphene-covered Ni metal substrate. (a) 3-D topography of bare Ni (2 × 2 μm²) metal obtained with AFM (contact mode) showing Ni grains surrounded by interface boundaries. (b) Friction force map measured on the same Ni region of panel (a) showing higher friction values (bright colour) at grain boundaries compared to Ni grains. (c) 3-D AFM topography image of a 5 × 5 μm² graphene region measured in contact mode. (d) Friction force map measured in parallel during the topography acquisition and obtained by the standard trace minus retrace technique (TMR). Direct comparison of panels (c) and (d) reveals that the IB region, which lies along the diagonal of the topography image, corresponds to the low friction region of the friction map.

Fig. 2 reveals comprehensive details of the same selected region of few-layer Gr/Ni–P under different instrumental set-up of optical microscope (panel (a)), Scanning Electron Microscope (SEM) (panel (b)), AFM topography (panel (c)) and friction force map (panel (d)). The optical contrast (Fig. 2(a)) corresponds to the reflection tendency of the surface and to variable graphene thickness. The bright colour correlates to few-layer graphene-covered Ni grain region while the IB regions appear relatively dark. The contrast on the SEM micrograph (Fig. 2(b)) of Gr/Ni–P shows the typical structure of this material composed of terraces, grain domains, IBs and step edges. The contrast image of SEM for Gr/Ni–P is the result of the amount of secondary electrons that are generated in the upper few nanometers of the sample surface. Further, a high secondary electron yield is expected for Ni as compared to carbon; Ni appears brighter in the SEM image.[33] Therefore, areas that result darker in the SEM image are the ones covered by a larger number of

graphene layers. The brighter contrast arises from secondary electrons that can still escape from underlying Ni substrate.

Fig. 2(c) is an AFM topographical view (15 × 15 μm²) in contact mode corresponding to the marked rectangle of panel (b); its topography data are presented using a local derivative in ESI, S1.† The large bright region in panels (a) and (b) corresponds to the flat area visible in the centre of the AFM image. While the darker regions correlate to IB regions which are greater in height than graphene layers and are rougher than grain regions. Inhomogeneous distribution of the graphene layers is dependent on orientation and size of Ni grains underneath, which produces different diffusion rate of carbon to the surface.[32]

Fig. 2(d) represents a friction force map measured on the same region of panel (c). The friction contrast reveals a high friction zone at the centre of the image which seems to correspond with the flat part of panel (c) while lower friction
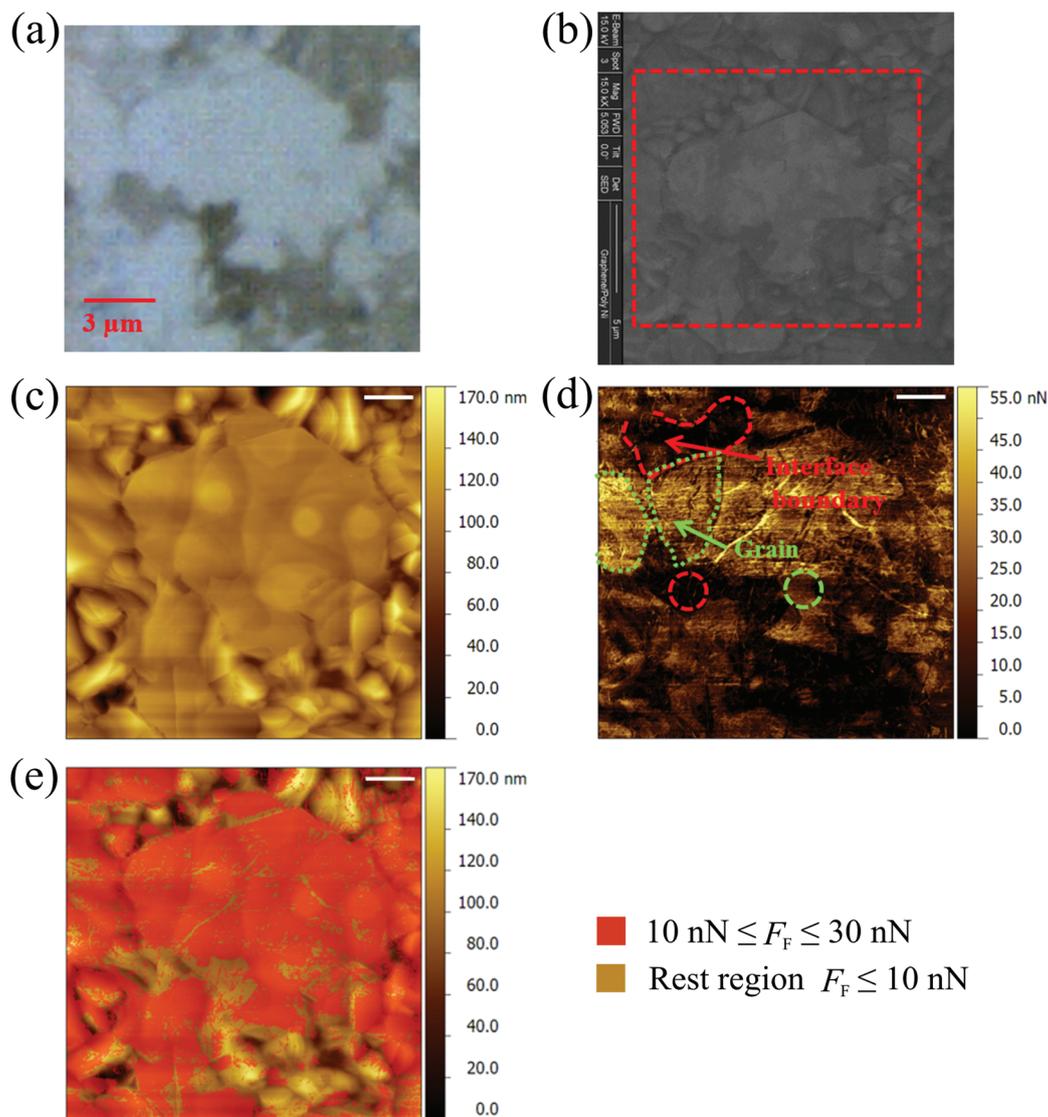
Fig. 2 Topology and friction map correlation for specific Gr/Ni–P region in optical microscope, SEM and AFM set-up. (a) Optical image (objective lens 50× resolution) ~ 15 × 15 μm² of Gr/Ni–P shows optical contrast due to variable graphene distribution from grain and IB. (b) SEM image (20 × 20 μm²); contrasts indicate different thickness of graphene films. Details are described in the text. (c) AFM topographic image (15 × 15 μm²) measured in contact mode (height channel) corresponding to marked region in panel (b). (d) Friction force map measured in parallel during the topography acquisition and obtained by TMR analysis. The encircled regions of green and red colours represent grains and IB respectively. (e) Overlapping of topography and friction map; the red dots represent areas characterized by friction force values between 10 and 30 nN.

signals are observed at surrounding of flat grains which are IBs. The topographical description of the encircled IB is mentioned in ESI, S2.† Fig. 2(e) shows overlapping of topographic and friction force mask having range 10–30 nN that clearly distinguishes friction force generated at grains and IBs.

Friction contrast under normal force F_N could also originate due to anisotropy in friction with graphene-covered polycrystalline Ni. The Ni domains are randomly oriented and epitaxial grown graphene follows a similar fashion.[32] F_L measurement is established as a powerful tool used to differentiate between grain and grain boundaries of metal foil like Cu,[18] Ni or Gr/Ni–P. Indeed, Marsden *at el.*[18] recently demonstrated the applicability of F_L map for better spatial resolution over SEM

imaging where F_L contrast occurs due to difference in thickness of graphene layers. It could also originate from differences in material interaction, *i.e.* contrast that arises from differences in chemical interaction between the sliding tip and the surface. Hence, colour contrast arising from F_L is not sufficient information to classify graphene thickness. The same region of Fig. 2 has been observed using a Raman spectrometer along with reference material like 1L graphene on silica and 1L graphene on Ni crystal (ESI, Fig. S3†). Raman laser was probed at two specific locations marked by dashed circles in Fig. 2(d) (area of nearly 1.4 μm²). The roughness (R_a) of these particular locations is 2.77 nm (for grain) and 8 nm (for IB region). Their Raman spectra are presented in ESI,

Fig. S3,† showing that IB are richer in carbon layers than grain regions. These collective results from roughness measurement and Raman analysis reveals that regions around IB are rich in carbon layers and have significant higher roughness that may cause lower contact area between sliding AFM probe and graphene. Therefore, F_L contrasts were influenced by thickness distribution and roughness of graphene layers.

Morphology influence on wettability of Gr/Ni–P

A single layer of graphene on Ni substrate shows pronounced impact on surface energy of the Gr–Ni system and increases its water contact angle (WCA) for a static water droplet, which is shown in Fig. 3. Bare Ni substrate shows the lowest WCA while graphite shows the highest value. Note that the presence of airborne contaminants upon exposure to ambient conditions[34] and the presence of native nickel oxide lead to finite contact angle on bare Ni surface (54.4 ± 6.4°), otherwise 0° has been reported for atomically clean Ni metal.[35] The measurements for WCA carried out on various substrates represent wettability influence from different number of graphene layers, substrate effect and morphology, including roughness.[36] One layer of graphene over Ni crystal enhances the WCA to 82.4 ± 3.2° compared to bare Ni metal. Here, our result does not support the wetting transparency theory[37] but it does follow the phenomenon of partial wetting transparency,[38] as WCA is comparable for 1 layer and 4–7 layer graphene, and is ∞ for HOPG. Li *et al.*[34] showed weak substrate dependence for CVD-produced graphene on Ni and Cu substrates using WCA values that are affected by airborne impurities. Fig. 3(b) shows the variation of work of adhesion (WA) between a water droplet and different samples evaluated by means of contact angle measurement and the Young–Dupré equation (see eqn (2)). The bare Ni metal

shows the highest WA of 115 mN m^{-1} relative to 1 L Gr/Ni(111), Gr/Ni–P and graphite, the values for which are ~82 mN m^{-1}, 74.7 mN m^{-1} and 73.2 mN m^{-1} respectively. These results indicate that less energy is required by a water droplet to separate from Gr/Ni sample but the lowest is in the case of graphite as also demonstrated elsewhere.[36,38]

The relation between WCA and roughness of carbon layers is shown in Fig. 3(c). It reveals that WCA value of Gr/Ni–P lies between those of single layer graphene and graphite. It might be possible that a little enhancement in WCA has been achieved through roughness of surface arising at IB of Gr/Ni–P. As described above, single layer graphene over Ni surface increases WCA but almost preserves the roughness ($R_a \approx$ 0.331 nm for bare Ni metal and $R_a \approx$ 0.220 nm for 1L Gr/Ni (111) crystal) of the substrate. Gr/Ni–P results in higher roughness of R_a = 7.5 nm especially at IB. 1L Gr/Ni (111) represents the system of zero area of IB while our current sample of FLG Gr/Ni–P has IB approximately covering 30.2% of an area of 20 × 20 μm^2 size (from Fig. 4(a)). This observation is shown in Fig. 4(a), where z-values (colour scale bar) from graphene-covered grain are subtracted with baseline correction treatment. Therefore, only the amplitude (z-direction) of carbon layers at IB is shown except a few humps at grain regions (amplitude <15 nm). The higher amplitude, *i.e.* from 15 nm to 75 nm, appears from the region of IB that acts as pillars and traces greater than 75 nm. These carbon pillars have a wide range of height distribution that is reflected in their roughness (R_a), Fig. 4(b). R_a is the average roughness measured from four different regions of area 10 μm^2 each (marked as I, II, III, IV in Fig. 4(a)). Similar measurement was carried out at grain regions that exclude pillars of IB. R_a of grains shows consistent values for Gr/Ni sample up to 20 μm^2 surface area, while it is
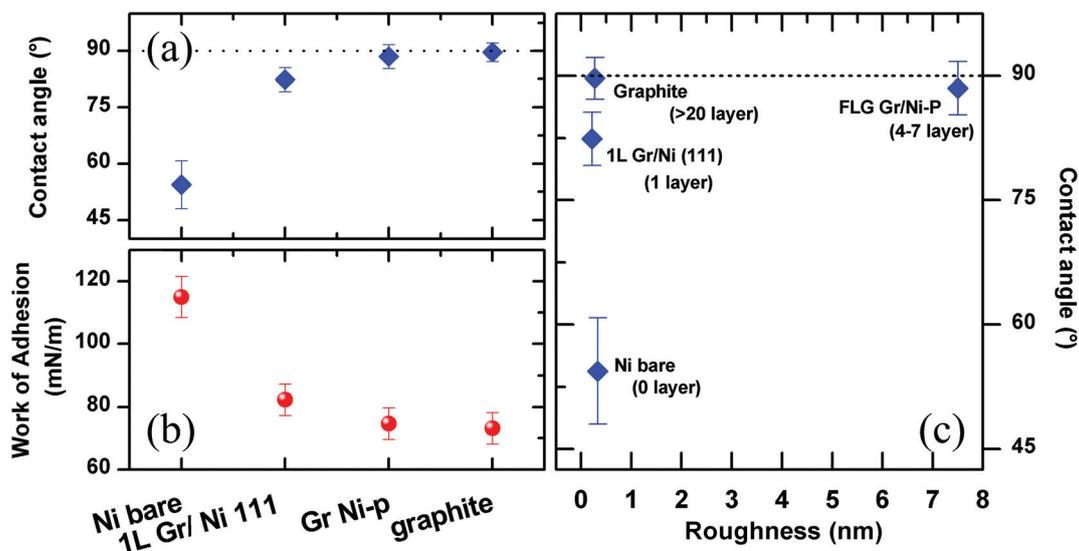
Fig. 3 Correlation between water contact angle and work of adhesion, and role of roughness of graphene layer(s). (a) Contact angle measurement using de-ionized water (~2 μL) on different substrates. WCA [°] decreases with increasing number of graphene layers and thus the highest value is for graphite. The error bars show the deviation of contact angle values from average. (b) WA between water and different substrates. The data have been taken from panel (a) and calculated through the Young–Dupré equation (see eqn (2)). (c) WCA related to roughness of the surface.
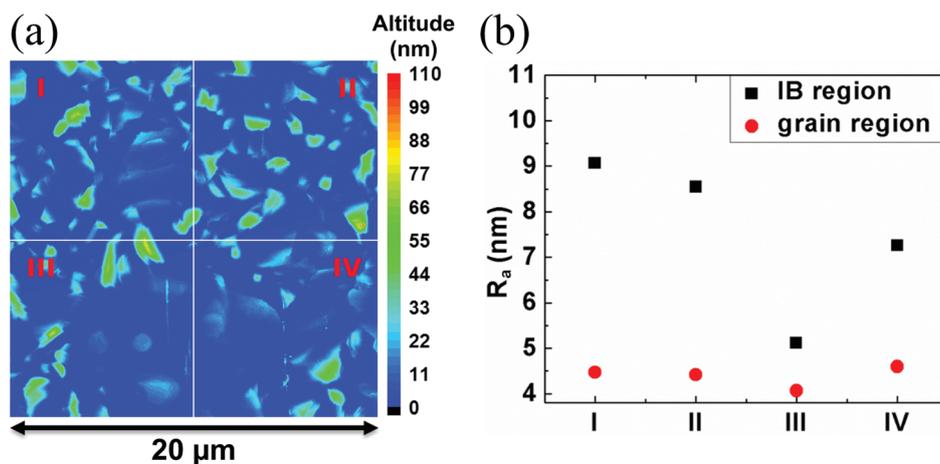
Fig. 4 Appearance of IB for Gr/Ni−P. (a) Base corrected followed by grain height subtraction AFM topography image (20 × 20 μm²) of Gr/Ni−P. It shows the majority of IB with greater height in the z-direction (>15 nm). It is divided in four different zones (I, II, III, IV) each of area 10 × 10 μm². (b) Plot of surface roughness (R_a) of the four different regions of IB and grain (for grain without base correction).

higher and fluctuates at the IB region. The surface area of graphene-covered grains is measured as 800 nm² to 1200 nm². It results in an aspect ratio (*i.e.* height of carbon layer at IB/separation distance of IB pillars on opposite side of a grain) of about 0.022–0.066, which is not sufficient to achieve pronounced WCA values.[39] But our current investigation evidences that using smaller metal grain size and/or enhancing the height of carbon layers at IB through controlled production may result in a textured surface with different wettability.

Morphological influence (grain and interfacial grain boundary) on friction characteristics

In order to measure friction force on a specific grain or on an IB, lower scale (few nanometers) inspection is necessary. Load-dependent friction measurements were carried out in vacuum (10^{-5} Torr) to avoid capillary forces[40] and the effect of airborne impurities. In this condition, friction measurement comprises only effects from sample morphology, graphene thickness and real contact condition between slider and topmost graphene layer. Fig. 5 shows load-dependent friction measurements from single grains, on an IB and HOPG. The measurement has been conducted by ceasing the slow scan movement of the cantilever while continuously scanning along the fast scan direction (about 100 nm). The physical advantage of this method is that the cantilever does not proceed and repeat its slide over the single line scan continuously. In this way friction data even from a relatively small IB region can be obtained. F_N was varied in the range from 38 nN to −22 nN by controlling the cantilever separation from the substrate. Here F_N = 0 nN stands for un-deflected cantilever, a situation where adhesion
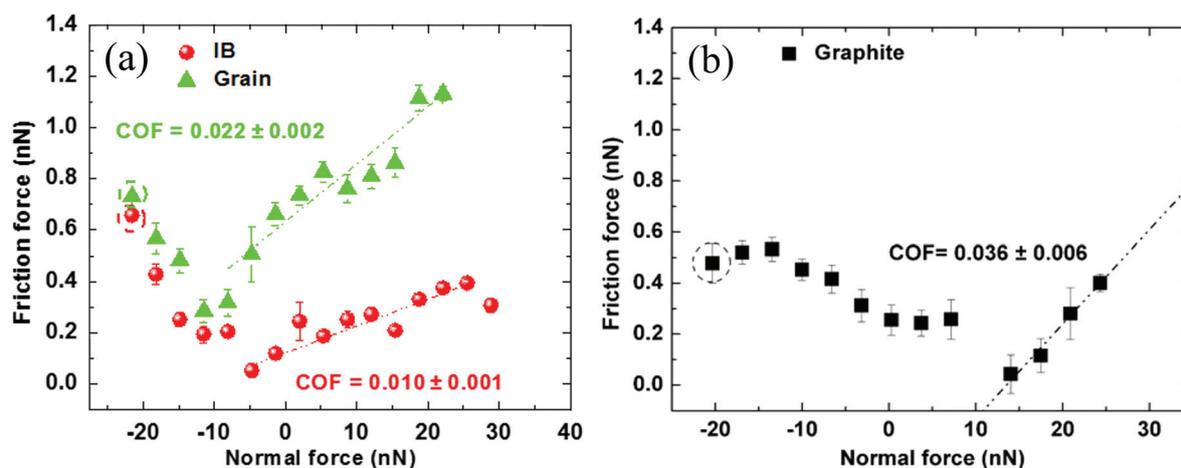
Fig. 5 Friction force at variable F_N from finite load until detachment for grain, IB and graphite. Load-dependent friction plot between silica tip and few-layer graphene on (a) Gr/Ni−P and (b) HOPG carried out in vacuum (10^{-5} Torr). Panel (a) shows load-dependent friction force for regions of grains and IB. Linear fit of the plot (during approach) is used to calculate COF (see text for details). The encircled values of F_N represent dynamic pull-off forces.

from surface gets neutralized by an applied normal deflection of the cantilever. Measurement is started by applying a higher deflection, and then it is sequentially decreased after 60 seconds until detachment point (where the tip gets separated from the surface). The overall measurement area covered was $\sim 100 \times 150$ nm^2.

The lowest value of F_N when the tip gets separated during lateral sliding is referred to as "dynamic pull-off force" encircled in Fig. 5. Its value in vacuum condition is nearly -22 nN for curves of both grain and IB in panel (a) and a close resemblance with graphite (≈ -20.7 nN) in panel (b). These values reflect the condition of sliding tip feeling similar adhesion during retraction whether from grains, IB or graphite. For all curves presented in Fig. 5, the friction force (F_F), calculated as the mean value of F_L over a grain, achieves lowest values around zero F_N and increases in either direction, whether the tip is progressing towards repulsive regime or is retracting from adhesive regime with respect to separation from the upper graphene layer. The error bar associated to each point is the standard deviation from the mean value of F_F.

In the following section we discuss the evolution of F_F for progression and retraction of the sliding tip for the adhesive and repulsive regime respectively. In the repulsive regime, a linear fit of the curve calculated as $\left(\dfrac{\partial F_F}{\partial F_N} \right)$ is defined as the COF. The COF measured in the repulsive regime for IB, grain, and graphite is measured as 0.010 ± 0.001, 0.022 ± 0.002, and 0.036 ± 0.006 respectively as shown in Fig. 5(a and b). The COF obtained from a grain region is nearly twice as much as that obtained from IB which demonstrates the lower friction characteristics of IB towards silica tip in vacuum condition. Nevertheless, the COF obtained for graphite is observed to be higher than those for both grain and IB. During retraction of the tip, the linear fit of the retraction part of the curve is referred to as a negative COF. The negative notion applies from the fact that F_N is acting in the reverse direction than it was in the repulsive regime. The $-$COF obtained from grains and IB is equal to about 0.03 ± 0.05, which is higher than the values obtained from graphite, 0.013 ± 0.030. This particular phenomenon has been described by Deng et al.[23] for graphite in air condition, and our results confirm this behaviour even in vacuum condition. Egberts et al.[19] observed a similar trend of friction curve during loading and unloading of a sliding tip apex for Gr–Cu system, where friction force is higher for unloading tip than loading. This occurs when adhesion between tip apex and topmost graphene layer(s) is higher than exfoliation energy of sub-surface. During retraction, the tip lifts the surface graphene layer(s) and locally separates them from the bulk. The lifted upper layer(s) are more susceptible to out-of-plane deformation than when they are firmly attached to the bulk. Deformed graphene resists the sliding motion of the cantilever owing to which cantilever records higher F_F.[24] In our previous work on single-layer graphene on Ni (111) crystal, we did not observe this effect and were unable to obtain $-$COF[30] which illustrates that single-layer graphene is strongly attached to Ni. The present investigation indicates that Ni

metal influences the graphene layer to a finite extent and might not be applicable for bulk (more than about ten). Nevertheless, a systematic study would be required in future to introduce graphene layers sequentially over Ni metal for measuring the extent of interfacial adhesion.

From Fig. 5, F_F at a particular $F_N = -20$ nN is recorded for all curves of graphite, IB and grain, observed as 0.47 nN, 0.53 nN and 0.66 nN respectively. The choice of $F_N = -20$ nN is taken due to its importance of being a retracting force just before the detachment of the cantilever. F_F value at $F_N = -20$ nN is related to the puckered size of graphene layer(s) in front of the sliding direction of the tip apex.[41] The strength of this pucker depends on the adhesion of the thin film to the substrate as described above. Higher F_F corresponds to greater size of puckered graphene that leads to out-of-plane deformation of layer(s), which is observed to be higher at grain regions ($F_F = 0.66$ nN). Here two phenomena are dominating. First, higher roughness at IB causes lower contact area at the interface unlike in graphite. Second, interfacial interaction between Ni metal and graphene is higher than interplanar weak vdW interactions in the upper layers of graphite. Therefore, for graphene-covered grain, the topmost layer has less interaction with its subsequent sheets that may provide higher susceptibility towards the slider. This effect has been shown by MD simulations, where inserted second graphene layer has less interaction with 1 L Gr–Ni (111) than on the slider.[27] This means that introducing more carbon layers can reduce the interfacial strength between topmost sheet and Ni substrate. Note that a free single layer of graphene has lower bending stiffness (proportional to the cube of the thickness according to continuum mechanics) than thicker carbon layers.[25] Raman spectra (ESI, S3 and S4†) showed that the number of graphene layers at grains is increased up to 4 times. Due to finite availability of the number of layers, upper thinner graphene sheet(s) might be available with weaker interplanar forces than usual, since the bottom layers are strongly interacting with the Ni substrate. This is in contrast to IB and graphite where thicker graphene layers are available and consequently a smaller puckered size.

Finite Element Method (FEM) simulation results are summarized in Fig. 6, showing the friction force (F_F) vs. normal load (F_N) curves, and vertical deflection for graphene on grain, IB and graphite for different regimes. F_F is determined as the average of the friction force recorded at the AFM tip for a displacement of 50 nm at a steady state stabilization after the initial acceleration of the tip. During approach activity of the tip, IB (red line) shows lower out-of-plane deformation that actually we can relate to higher roughness than at grains. At the withdrawing stage, simulation confirms the general trend experimentally observed of an increase in the friction force: this is clearly related to higher deformability that graphene layers show since the weaker interaction, and then restrain, as they are moved away from the substrate. The weaker interaction is also demonstrated by the higher area for adhesion of graphene on the tip on grains and at pull-out. The top layer of graphite deforms significantly compared to lower layers, and

(a)

COF = -0.045 ± 0.0093
COF = -0.035 ± 0.0019
COF = -0.037 ± 0.0068

COF = 0.032 ± 0.0018
COF = 0.022 ± 0.0016
COF = 0.010 ± 0.0012

▲ Graphene on grain   ● Graphene on IB   ■ Graphite

(b) **(c)**
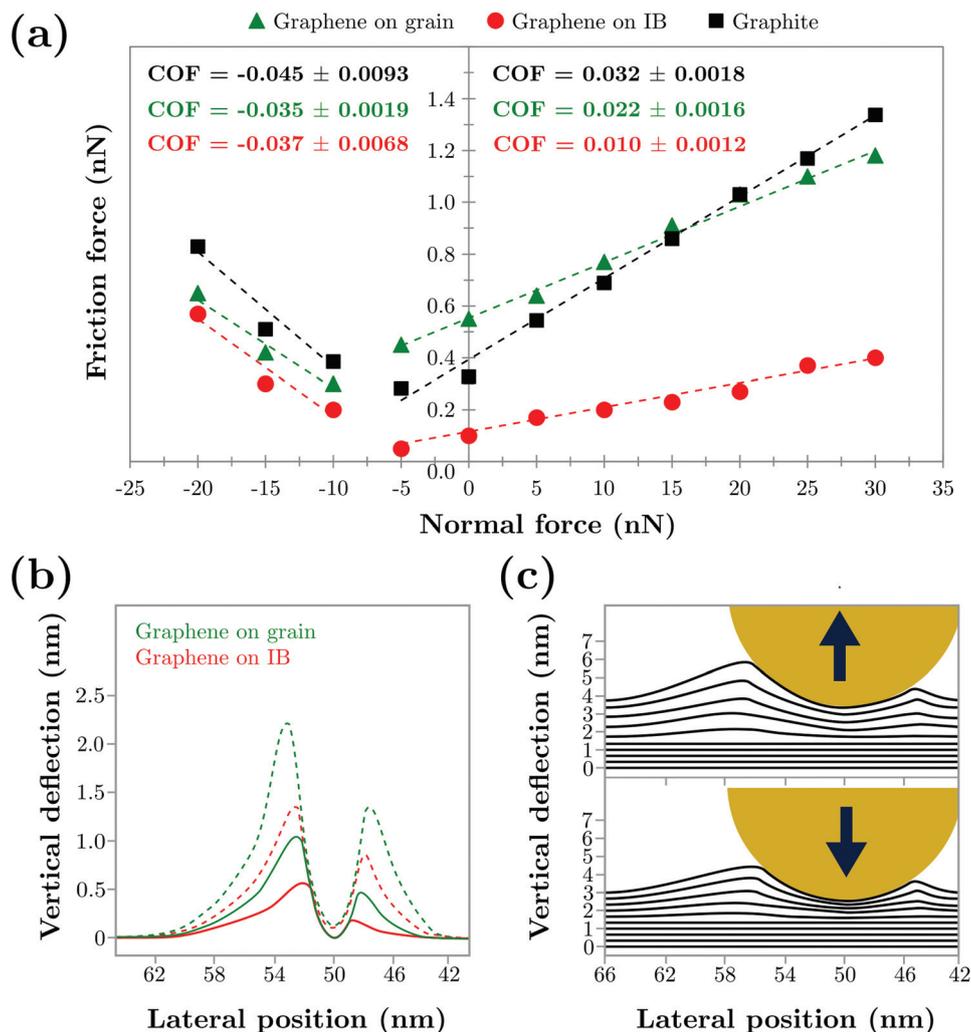
Fig. 6 Results of finite element friction simulations. (a) F_F vs. F_N results from FEM simulation on graphene-covered grain, interfacial grain boundary, and graphite with estimation of the coefficient of friction for the two identified regimes. (b) Plot of the vertical deflection for single-layer graphene on grain and interfacial grain boundaries corresponding to a load of +15 nN and −15 nN (negative load case corresponds to the dashed line), tip sliding towards the left-hand side, as noticeable from the asymmetric deformed shape. (c) Plot of the vertical deflection of graphite in the two different regimes (−15 nN and +15 nN).

the deformation occurs in the top 3–4 layers. The COFs obtained from linear fit of load-dependent friction curves during approach of the tip are moreover in good agreement with experimental results. At withdrawing event, a higher value of F_F at puckering is recorded for graphite.

In continuation of FFM experiments, normal force-displacement ($F_{N\text{-}\delta}$) measurements were performed at the end of each set of friction measurements to calculate the static pull-off force. Unlike dynamic pull-off force, the tip vertically approaches the surface and then retracts back, without any lateral movement. Therefore, this part of the experiment explains the static adhesion force between tip and carbon atoms beneath it. The pull-off values obtained from $F_{N\text{-}\delta}$ curve for grain and IB are −17.6 ± 0.6 nN and −15.2 ± 0.15 nN respectively. Work of adhesion, γ (i.e. work per unit area required to separate the surfaces from contact to infinity) was calculated using the DMT (Derjaguin–Müller–Toporov) approximation. The interaction between AFM probe and graphene on Ni corresponds to long-range adhesion between harder materials as observed in our previous work[30] and from the literature.[44] The following DMT relation between pull-off force ($F_{\text{pull-off}}$) and the work of adhesion (γ) has been considered:[42]

$$\gamma = \frac{-(F_{\text{Pull-off}})}{2\pi R} \tag{1}$$

where R is the tip radius ($\approx 8 \pm 3$ nm); thus γ for grain and IB is calculated as ≈ 290 mN m^{-1} or 0.29 J m^{-2} and ≈ 250 mN m^{-1} or 0.25 J m^{-2} respectively. Our data show that γ decreases when roughness increases at the interface, as reported by Jacobs and coworkers.[43]

These values of static pull-off force are lower than dynamic pull-off force values obtained during sliding experiments. The discrepancy in values for "static" and "dynamic" pull-off forces is due to the fact that dynamic pull-off force occurred at deformed graphene where sliding history of the tip apex plays an essential role.[41] As described, we started our measurement at higher F_N and sequentially decreased over same graphene layer at intervals of 60 seconds until detachment. Therefore, before detachment of the cantilever, the tip apex slides over the same graphene layer between 13 and 15 minutes with varying load. This process locally deforms graphene at each interval and retraction of the tip can lift the graphene layer(s) and locally separate them from the bulk. The lifted and puckered graphene leads to higher vertical deflection of the cantilever and hence higher pull-off force.[41] While for static pull-off force, such higher deformation might not be available due to absence of sliding history, and puckering might occur due to adhesion of carbon atoms.

The effect of sliding history can be avoided through reversing the direction of F_N, which can be achieved by starting F_N with lower load just before the detachment point ($F_N \approx -10$ nN) and sequentially increasing its value. Fig. 7 shows load-dependent friction for graphite, grain and IB. The COF of the repulsive regime for IB, grain and graphite is 0.01 ± 0.003, 0.01 ± 0.009 and 0.033 ± 0.002 respectively, similar to the results presented in Fig. 5 and 6. For the grain region, the slope is similar to that of the IB and these slope values are at the limit of the resolution of our instrument. Nevertheless, the friction force recorded is higher than that obtained for IB. In the adhesive regime at $F_N \approx -5$ to 10 nN, F_F is higher for graphite than for grain and lowest for IB, which indicates

higher adhesion between graphite and the tip apex and subsequently lowering towards IB following the grain region. Graphene layer(s) is not deformed significantly in the beginning, and the obtained F_F values are from adhesion between tip apex and graphene carbon atoms. Obviously, higher roughness leads to lower contact area at IB resulting in lower F_F.[16,44] The magnitudes of F_F shown in Fig. 5 and 7 are not comparable in the adhesive regime, since in the former case friction data were affected by the sliding history as deformed graphene of unknown puckered size. While in the latter case, the adhesion between graphene and tip occurred with minimal deformation. Fig. 5 and 7 indicate that sliding history plays a vital role for frictional characteristics of graphene in the adhesive regime during retraction of the tip. Nevertheless, the influence is insignificant for FLG structure, like IB and graphite in the repulsive regime. Graphene friction against the silica tip showed reproducible results in the repulsive regime with and without involvement of sliding history.

The frictional characteristics of Gr/Ni–P have been compared with those of some reference systems, namely 1L graphene on Ni (111), graphite and bare Ni metal. Their respective COFs (determined in repulsive regime) are reported in Fig. 8. These results were obtained in similar conditions to vacuum (10^{-5} Torr) with the same experimental set-up. The scatter plot was based on repeated measurements over the same sample. It is clearly shown that frictional characteristics of graphene are substrate dependent whether it may be Ni (111), a few layers over polycrystalline (that includes subsection of grain and IB) and graphite. The stronger interaction between native oxides of silicon tip and Ni metal (SiO_2–NiO_x) led to the highest COF, which is nearly 50 times lower for a single graphene layer over Ni (111). IB has a lower COF than

Fig. 7 Load-dependent friction curves to minimize sliding history of cantilever. Load-dependent friction in vacuum (10^{-5} Torr) for graphene-covered Ni IB and graphite. The applied displacement started from $F_N = -10$ nN and sequentially increased in order to avoid sliding history of the tip over the same graphene layer(s). The COF of the linear part of the repulsive regime for IB, grain and graphite is 0.01 ± 0.003, 0.01 ± 0.009 and 0.033 ± 0.002 respectively.

Fig. 8 Coefficient of friction for varying graphene layer distribution and morphology. Coefficient of friction (COF) from experiments for Gr/Ni–P along with reference samples, namely 1 L Gr/Ni (111), graphite and bare Ni–P metal. The COF has been obtained through linear fit of curves of F_F vs. F_N recorded at the AFM tip. Each point represents a set of measurements and encircled region shows COF for IB.

grain and even comparable with 1 L graphene on Ni (111). This means that the lowest COF could be achieved through enhancement of roughness of graphene layers. Our investigation shows that integral effect from grain and IB for Gr/Ni–P causes a significant drop in COF compared to graphite as shown by Kim *et al.*[16] at the microscale at air condition. Our measurement at air conditions shows COFs for IB and grain obtained are 0.011 ± 0.195 and 0.018 ± 0.018 respectively. These values are comparable with those obtained in vacuum and further validate the absence of capillary effect or airborne impurities at least up to 8 hours. Introducing higher density of IB might further decrease COF, and similar value would be achieved as equivalent to 1 L graphene on Ni (111). This may lead to more applications, since polycrystalline metals are more cost effective than pure crystals.

Conclusion

The higher accumulation of carbon layers at IB than at grains (revealed by Raman spectra) may regulate tribological characteristics of the substrate. CVD-produced 1L graphene over Ni (111) resulted in significantly lower surface energy as shown in the work of adhesion calculations. Gr/Ni–P offers higher WCA due to involvement of randomly oriented few-layer graphene with enhanced roughness from IB. IB roughness provides a condition of textured surface with carbon pillars/spikes, where the aspect ratio is nearly 0.014–0.02 in the current study. Load-dependent friction measurements carried out in vacuum (10^{-5} Torr) reveal that sliding history plays an important role in producing puckered graphene that strongly affects the friction force (F_F) values in the adhesive regime (when the tip apex is close to detachment point). Graphene covering grain and IB reduces COF, where it is nearly half at IB than at grain. COF values obtained for graphene-covered grain and IB in vacuum and air conditions are similar at least up to 8 hours of exposure to air condition. This shows Gr/Ni–P is not affected by airborne impurities and the capillary effect for this duration. Roughness at IB produces favourable condition for the AFM tip to achieve lower F_F due to a decrease in real contact area at the interface, which was absent in the reference HOPG material used. Finite element simulations mimicking the experimental conditions identify the role of out-of-plane deformation of 1L and FLG in tuning the lateral force and friction. The COF values numerically calculated are in good agreement with experimental results.

Graphene frictional characteristics depend on its out-of-plane bending stiffness. Stiffer graphene has lower susceptibility toward the slider due to high resistance for out-of-plane deformation (*e.g.* Gr/Ni (111)). It is established that for weaker interaction between the graphene and the substrate (*e.g.* silica substrate), F_F is higher for a single layer but decreases with increasing number of layers due to the higher resistance to the out-of-plane deformation.[21] Our observation from FFM measurements in vacuum (10^{-5} Torr) shows that this fact might not be applicable for material interacting strongly with graphene. Moreover, there are other factors like roughness, interaction between graphene layers, and separation distance from Ni substrates that also play a vital role. Introducing a limited increment of graphene layers over Ni surface (*e.g.* grain regions) might produce a weaker interaction with the topmost layer since bottom layers are strongly interacting with metal (only applicable for few layers, up to 4). The availability of upper layers with limited interaction with the substrate, and thus with lower stiffness, leads to higher puckering, and consequently higher F_F. Therefore, resistance to out-of-plane deformation for graphene is the key element to minimize F_F in FFM measurements. The phenomenon of obtaining stiffer graphene should be through its subsurface not over it, as shown by functionalized graphene through fluorination[34] or hydrogenation,[35] leading to higher friction force. Thus, an alternative way was shown to minimize F_F for CVD-produced graphene through its enhanced roughness resulting from interfacial grain boundary of Ni metal. Our study is applicable for all types of metal foil where graphene is partially or fully dissolved during its production.

Method

Materials

Gr/Ni–P is a multilayer graphene film supported on polycrystalline nickel, grown by CVD.[45] It is a commercial sample obtained from Graphene Laboratories Inc. NY, United States (Graphene supermarket). Before starting the experiment the Gr/Ni–P sample was subjected to a sequential cleaning procedure with acetone and isopropyl alcohol in an ultrasonic bath for 30 minutes at 50 °C. Then the Gr/Ni–P sample was heated in an external oven at 430 °C in argon flux to remove the residual impurities. The sample was inserted in the AFM set-up and loaded on a temperature-controlled heater stage (Enviroscope P/N: ESHTH, controlled by a Nanoscope IV unit). The AFM chamber is connected with a turbomolecular pump and an oil-free scroll vacuum pump to carry out measurements in high vacuum. Before each set of measurements the Gr/Ni–P sample was heated inside the AFM chamber in vacuum condition up to 250 °C for 2 hours. Friction measurement was started after sample cooling to room temperature and not more than 14 hours before heat treatment. Vacuum condition (10^{-5} Torr) was maintained from the moment of heating of the sample. Nine measurements in total were carried out in vacuum condition under same instrumental set-up. All plots and COF values are reported in Fig. 5, 7 and 8 with support of FEM simulations.

Instrumentation and calibration procedure

Graphene sample has been investigated with different techniques as follows. SEM (FEI NOVA NanoSem at 5 kV) and AFM in tapping mode (Enviroscope system by VEECO) were used for topographical analysis. Raman spectroscopy (Horiba, Jobin-Yvon spectrometer, model Labram, 632.8 nm wavelength, spot diameter ∼ 1 μm) has been carried out to measure the graphene thickness for the Gr/Ni sample. The same set-up has

been used to analyze CVD-produced graphene on Ni foil and transferred to silica substrate (Gr/SiO$_2$-T). Friction force measurement has been carried out with the same AFM apparatus operated in contact mode in vacuum condition (10^{-5} Torr). Commercially available silicon tips (MikroMasch model no. CSC37/noAl) covered with native oxide have been used for the topographic analysis as well as for friction measurement. Force–displacement (F–D) curves were systematically acquired to measure the sensitivity of the photodetector that allows conversion of units from volts to nanometers using the slope of the retraction part of the curve. The comprehensive details of this standard procedure can be found elsewhere.[46] The bending and torsional spring constants of the cantilever have been calculated through the Sader method.[47,48] Typical values are in the range of 0.3–0.4 N m^{-1} for the bending stiffness and $(2–5) \times 10^{-8}$ N m for the torsional one. Friction force (F_L) signal corresponds to the twisting of the cantilever during scanning which is deduced from the lateral photodetector voltage following the procedure described in references[46,49] with the assumption of a circular shape of laser beam on the photodetector. In that calculation, lateral sensitivity of the photodetector was assumed to be equal to the sensitivity measured during normal bending of the cantilever.

The sliding of the AFM tip produces lateral force on the cantilever that causes its lateral deflection in either direction (trace/retrace). The lateral signal in AFM is coupled with surface topography and induces an artefact. To minimize the topographic influence from the sample, trace and retrace scanning direction of the tip is subtracted, giving half of TMR; we refer to it as "lateral force" (F_L) and the mean value of F_L for a defined area as "friction force" (F_F). The advantage of this approach is to minimize topological influence from the substrate during friction analysis. Experimentally, it is the width of the lateral deflection loop in trace and retrace direction of the cantilever.[18] Multiple sets of measurements have been carried out through different cantilevers (similar configurations) with the same calibration procedure as described above.

The static contact angle was measured using a home-made system equipped with high-resolution dispenser and with a CMOS camera. The measurement has been performed using a 2 µL droplet of de-ionized water through image analysis.[50] Five sets of measurements have been carried out for each sample, estimating the mean values and the standard deviations. The work of adhesion of the surface was calculated using the contact angle by means of Young–Dupré equation as follows:

$$W_A = \gamma_{lv}(1 + \cos \theta) \qquad (2)$$

where W_A is the work of adhesion, γ_{lv} is the water's total surface tension (72.8 mJ m^{-1}) and θ is the contact angle.[51]

Finite element simulations

We performed 3D FEM numerical simulations reproducing the FFM experiments in order to understand the role of the surface roughness in the adhesion of graphene sheets on Ni substrate and, consequently, in the frictional properties of the

system. The planar extension of the modelled system was of 100×100 nm^2 both for graphene on Ni substrate and for graphite simulations (see ESI Fig. S5†). The tip was modelled as a hemispherical body with its radius equal to 8 nm, set according to the producer's specifications. The graphene layers and the substrate were fully clamped at the edges, and the Ni substrate at the bottom as well. The silica tip and the nickel substrate were modelled with solid elements. Tip, graphene sheets, and Ni substrate bodies were governed by isotropic linear elastic strain energies. Elastic properties, Young's modulus and Poisson's ratio, respectively, have been assumed for the silica tip: $E_{tip} = 170$ GPa and $\nu_{tip} = 0.2$, with density $\rho_{tip} = 2.300$ g cm^{-3}; for the nickel substrate: $E_{sub} = 200$ GPa and $\nu_{sub} = 0.31$ with density $\rho_{sub} = 8.908$ g cm^{-3}. The graphene sheets were modelled with fully integrated shells (2×2 Gauss point) based on the Reissner–Mindlin kinematic assumption. Nominal elastic properties of graphene were assumed to be Young's modulus $E_g = 1$ TPa, $\nu_g = 0.2$ and $\rho_g = 1.300$ g cm^{-3}. However, in order not to overestimate the transverse flexural stiffness of graphene in continuum models it is acknowledged that an appropriate scaling of the graphene thickness and Young's modulus is necessary. The FEM results matched the experimental observations, using a reduced thickness of 0.066 nm, as used also by other authors for single-layer graphene[23,52] or single-walled nanotubes.[53,54] Consequently, the elastic modulus must be scaled up to an effective value of 5.5 TPa.

The differences in roughness were considered in the FEM model with an equivalent sinusoidal surface of equation $z = A \sin(\lambda x)\cos(\lambda y)$, in which A and λ are assumed to have equal values to the average surface roughness R_a and $1/4R_a$ respectively. The interactions between the graphene layers, graphene and substrate, tip and graphene sheet have been implemented via a cohesive zone-based model. The contact parameters (normal and tangential limit stress) were derived from Lennard-Jones 6–12 potentials according to Jiang et al.[55] analogously to the method reported by Deng et al.[23] Local static and dynamic friction coefficients between graphene layers, tip and substrate have been set to zero in the contact.

The simulation consisted of two main steps: (1) the normal force F_N was applied on the tip until the flat sheets reach their equilibrium configuration on the rough substrate via dynamic relaxation; (2) tip sliding through an imposed horizontal displacement. This displacement was imposed on an auxiliary node linked to the top of the tip hemisphere via a linear horizontal spring of rigidity $k = 10$ J m^{-2}. The friction force F_F was measured from the force recorded in the spring. In order to avoid boundary effects, the displacement domain of the tip was limited, keeping a distance between its apex and the boundaries at least of 25 nm (50 nm of overall tip excursion).

Acknowledgements

References

1 A. K. Geim and K. S. Novoselov, The rise of graphene, *Nat. Mater.*, 2007, **6**, 183–191.

2 A. H. Castro Neto, F. Guinea, N. M. R. Peres, K. S. Novoselov and A. K. Geim, The electronic properties of graphene, *Rev. Mod. Phys.*, 2009, **81**, 109–162.

3 J. Wintterlin and M. L. Bocquet, Graphene on metal surfaces, *Surf. Sci.*, 2009, **603**, 1841–1852.

4 Y. Kim, J. Lee, M. S. Yeom, J. W. Shin, H. Kim, Y. Cui, J. W. Kysar, J. Hone, Y. Jung, S. Jeon and S. M. Han, Strengthening effect of single-atomic-layer graphene in metal-graphene nanolayered composites, *Nat. Commun.*, 2013, **4**, 2114.

5 A. Klemenz, L. Pastewka, S. G. Balakrishna, A. Caron, R. Bennewitz and M. Moseler, Atomic scale mechanisms of friction reduction and wear protection by graphene, *Nano Lett.*, 2014, **14**, 7145–7152.

6 S. Bae, H. Kim, Y. Lee, X. Xu, J.-S. Park, Y. Zheng, J. Balakrishnan, T. Lei, H. Ri Kim, Y. I. Song, Y.-J. Kim, K. S. Kim, B. Ozyilmaz, J.-H. Ahn, B. H. Hong and S. Iijima, Roll-to-roll production of 30-inch graphene films for transparent electrodes, *Nat. Nanotecnol.*, 2010, **5**, 574–578.

7 C. Chen, S. Rosenblatt, K. I. Bolotin, W. Kalb, P. Kim, I. Kymissis, H. L. Stormer, T. F. Heinz and J. Hone, Performance of monolayer graphene nanomechanical resonators with electrical readout, *Nat. Nanotecnol.*, 2009, **4**, 861–867.

8 A. K. Geim, Graphene: status and prospects, *Science*, 2009, **324**, 1530–1534.

9 S. Wang, Y. Zhang, N. Abidi and L. Cabrales, Wettability and surface free energy of graphene films, *Langmuir*, 2009, **25**, 11078–11081.

10 J. R. Felts, A. J. Oyer, S. C. Hernandez, K. E. Whitener Jr., J. T. Robinson, S. G. Walton and P. E. Sheehan, Direct mechanochemical cleavage of functional groups from graphene, *Nat. Commun.*, 2015, **6**, 6467.

11 G. H. Lee, R. C. Cooper, S. J. An, S. Lee, A. van der Zande, N. Petrone, A. G. Hammerberg, C. Lee, B. Crawford, W. Oliver, J. W. Kysar and J. Hone, High-strength chemical-vapor-deposited graphene and grain boundaries, *Science*, 2013, **340**, 1073–1076.

12 C. Lee, X. Wei, J. W. Kysar and J. Hone, Measurement of the Elastic Properties and Intrinsic Strength of Monolayer Graphene, *Science*, 2008, **321**, 385–388.

13 Y. J. Shin, R. Stromberg, R. Nay, H. Huang, A. T. S. Wee, H. Yang and C. S. Bhatia, Frictional characteristics of exfoliated and epitaxial graphene, *Carbon*, 2011, **49**, 4070–4073.

14 M. H. Muser and D. Shakhvorostov, Why Thick Can Be Slick, *Science*, 2010, **328**, 52–53.

15 D. Berman, A. Erdemir and A. V. Sumant, Graphene: a new emerging lubricant, *Mater. Today*, 2014, **17**, 31–42.

16 K. S. Kim, H. J. Lee, C. Lee, S. K. Lee, H. Jang, J. H. Ahn and J. H. Kim, Chemical vapor deposition-grown graphene: the thinnest solid lubricant, *ACS Nano*, 2011, **5**, 5107–5114.

17 T. Filleter, J. McChesney, A. Bostwick, E. Rotenberg, K. Emtsev, T. Seyller, K. Horn and R. Bennewitz, Friction and Dissipation in Epitaxial Graphene Films, *Phys. Rev. Lett.*, 2009, **102**, 086102.

18 A. J. Marsden, M. Phillips and N. R. Wilson, Friction force microscopy: a simple technique for identifying graphene on rough substrates and mapping the orientation of graphene grains on copper, *Nanotechnology*, 2013, **24**, 255704.

19 P. Egberts, G. H. Han, X. Z. Liu, A. T. C. Johnson and R. W. Carpick, Frictional Behavior of Atomically Thin Sheets: Hexagonal-Shaped Graphene Islands Grown on Copper by Chemical Vapor Deposition, *ACS Nano*, 2014, **8**, 5010–5021.

20 D. Berman, A. Erdemir, A. V. Zinovev and A. V. Sumant, Nanoscale friction properties of graphene and graphene oxide, *Diamond Relat. Mater.*, 2015, **54**, 91–96.

21 C. Lee, Q. Li, W. Kalb, X. Z. Liu, H. Berger, R. W. Carpick and J. Hone, Frictional characteristics of atomically thin sheets, *Science*, 2010, **328**, 76–80.

22 T. Filleter and R. Bennewitz, Structural and frictional properties of graphene films on SiC(0001) studied by atomic force microscopy, *Phys. Rev. B: Condens. Matter*, 2010, **81**, 155412.

23 Z. Deng, A. Smolyanitsky, Q. Li, X.-Q. Feng and R. J. Cannara, Adhesion-dependent negative friction coefficient on chemically modified graphite at the nanoscale, *Nat. Mater.*, 2012, **11**, 1032–1037.

24 A. Smolyanitsky, J. P. Killgore and V. K. Tewary, Effect of elastic deformation on frictional properties of few-layer graphene, *Phys. Rev. B: Condens. Matter*, 2012, **85**, 035412.

25 Q. Li, C. Lee, R. W. Carpick and J. Hone, Substrate effect on thickness-dependent friction on graphene, *Phys. Status Solidi B*, 2010, **247**, 2909–2914.

26 S. Das, D. Lahiri, D.-Y. Lee, A. Agarwal and W. Choi, Measurements of the adhesion energy of graphene to metallic substrates, *Carbon*, 2013, **59**, 121–129.

27 S. Cahangirov, S. Ciraci and V. O. Özçelik, Superlubricity through graphene multilayers between Ni(111) surfaces, *Phys. Rev. B: Condens. Matter*, 2013, **87**, 205428.

28 S. Kwon, J.-H. Ko, K.-J. Jeon, Y.-H. Kim and J. Y. Park, Enhanced Nanoscale Friction on Fluorinated Graphene, *Nano Lett.*, 2012, **12**, 6043–6048.

29 Y. Dong, X. Wu and A. Martini, Atomic roughness enhanced friction on hydrogenated graphene, *Nanotechnology*, 2013, **24**, 375701.

30 G. Paolicelli, M. Tripathi, V. Corradini, A. Candini and S. Valeri, Nanoscale frictional behavior of graphene on SiO 2 and Ni(111) substrates, *Nanotechnology*, 2015, **26**, 055703.

31 H. Hölscher, D. Ebeling and U. Schwarz, Friction at Atomic-Scale Surface Steps: Experiment and Theory, *Phys. Rev. Lett.*, 2008, **101**, 246105.

32 Y. Zhang, L. Gomez, F. N. Ishikawa, A. Madaria, K. Ryu, C. Wang, A. Badmaev and C. Zhou, Comparison of Graphene Growth on Single-Crystalline and Polycrystalline Ni by Chemical Vapor Deposition, *J. Phys. Chem. Lett.*, 2010, **1**, 3101–3107.

33 J. H. Warner, F. Schäffel, A. Bachmatiuk and M. H. Rümmeli, *Graphene fundamentals and emergent applications*, Elsevier, Amsterdam, New York, 2013, pp. 229–332.

34 Z. Li, Y. Wang, A. Kozbial, G. Shenoy, F. Zhou, R. McGinley, P. Ireland, B. Morganstein, A. Kunkel, S. P. Surwade, L. Li and H. Liu, Effect of airborne contaminants on the wettability of supported graphene and graphite, *Nat. Mater.*, 2013, **12**, 925–931.

35 R. Raj, S. C. Maroo and E. N. Wang, Wettability of Graphene, *Nano Lett.*, 2013, **13**, 1509–1515.

36 J. Zang, S. Ryu, N. Pugno, Q. Wang, Q. Tu, M. J. Buehler and X. Zhao, Multifunctionality and control of the crumpling and unfolding of large-area graphene, *Nat. Mater.*, 2013, **12**, 321–325.

37 J. Rafiee, X. Mi, H. Gullapalli, A. V. Thomas, F. Yavari, Y. Shi, P. M. Ajayan and N. A. Koratkar, Wetting transparency of graphene, *Nat. Mater.*, 2012, **11**, 217–222.

38 D. Kim, N. M. Pugno, S. Buehler and M. J. Ryu, Solving the Controversy on the Wetting Transparency of Graphene, *Sci. Rep.*, 2015, **5**, 15526.

39 R. Seemann, M. Brinkmann, E. J. Kramer, F. F. Lange and R. Lipowsky, Wetting morphologies at microstructured surfaces, *Proc. Natl. Acad. Sci. U. S. A.*, 2005, **102**, 1848–1852.

40 M. Binggeli and C. M. Mate, Influence of capillary condensation of water on nanotribology studied by force microscopy, *Appl. Phys. Lett.*, 1994, **65**, 415–417.

41 X.-Z. Liu, Q. Li, P. Egberts and R. W. Carpick, Nanoscale Adhesive Properties of Graphene: The Effect of Sliding History, *Adv. Mater. Interfaces*, 2014, **1**, 1300053.

42 R. W. Carpick, D. F. Ogletree and M. A. Salmeron, General Equation for Fitting Contact Area and Friction vs Load Measurements, *J. Colloid Interface Sci.*, 1999, **211**, 395–400.

43 T. D. B. Jacobs, K. E. Ryan, P. L. Keating, D. S. Grierson, J. A. Lefever, K. T. Turner, J. A. Harrison and R. W. Carpick, The Effect of Atomic-Scale Roughness on the Adhesion of Nanoscale Asperities: A Combined Simulation and Experimental Investigation, *Tribol. Lett.*, 2013, **50**, 81–93.

44 Z. Burton and B. Bhushan, Hydrophobicity, adhesion, and friction properties of nanopatterned polymers and scale dependence for micro- and nanoelectromechanical systems, *Nano Lett.*, 2005, **5**(8), 1607–1613.

45 F. Güneş, G. H. Han, K. K. Kim, E. S. Kim, S. J. Chae, M. H. Park, H.-K. Jeong, S. C. Lim and Y. H. Lee, Large-area graphene based flexible trensparent conducting films, *Nano*, 2009, **04**, 83–90.

46 R. W. Carpick and M. Salmeron, Scratching the Surface: Fundamental Investigations of Tribology with Atomic Force Microscopy, *Chem. Rev.*, 1997, **97**, 1163–1194.

47 J. E. Sader, J. W. M. Chon and P. Mulvaney, Calibration of rectangular atomic force microscope cantilevers, *Rev. Sci. Instrum.*, 1999, **70**, 3967.

48 C. P. Green, H. Lioe, J. P. Cleveland, R. Proksch, P. Mulvaney and J. E. Sader, Normal and torsional spring constants of atomic force microscope cantilevers, *Rev. Sci. Instrum.*, 2004, **75**, 1988.

49 D. Bachmann and C. Hierold, Determination of pull-off forces of textured silicon surfaces by AFM force curve analysis, *J. Micromech. Microeng.*, 2007, **17**, 1326–1333.

50 A. F. Stalder, G. Kulik, D. Sage, L. Barbieri and P. Hoffmann, A snake-based approach to accurate determination of both contact points and contact angles, *Colloid Surf., A*, 2006, **286**, 92–103.

51 R. P. S. Chakradhar and V. Dinesh Kumar, Water-repellent coatings prepared by modification of ZnO nanoparticles, *Spectrochim. Acta, Part A*, 2012, **94**, 352–356.

52 F. Scarpa, S. Adhikari, A. J. Gil and C. Remillat, The bending of single layer graphene sheets: the lattice versus continuum approach, *Nanotechnology*, 2010, **21**, 125702.

53 B. I. Yakobson, C. J. Brabec and J. Bernholc, Nanomechanics of Carbon Tubes: Instabilities beyond Linear Response, *Phys. Rev. Lett.*, 1996, **76**, 2511–2514.

54 A. Pantano, D. M. Parks and M. C. Boyce, Mechanics of deformation of single and multi walled carbon nanotubes, *J. Mech. Phys. Solids*, 2004, **52**, 789–821.

55 L. Y. Jiang, Y. Huang, H. Jiang, G. Ravichandran, H. Gao, K. C. Hwang and B. Liu, A cohesive law for carbon nanotube/polymer interfaces based on the van der Waals force, *J. Mech. Phys. Solids*, 2006, **54**, 2436–2452.

Tribological characteristics of few layers graphene over Ni grain and interface boundaries

Electronic Supplementary Information (ESI)

M. Tripathi[1], F. Awaja[1], G. Paolicelli[2], R. Bartali[1], E. Iacob[1], S. Valeri[3], S. Ryu[4], S. Signetti[5], G. Speranza[1], N.M. Pugno[5,1,6,*]

[1] Centre for Materials and Microsystems, Fondazione Bruno Kessler, via Sommarive 18, I-38123 Povo (Trento), Italy

[2] Istituto Nanoscienze, Consiglio Nazionale delle Ricerche, via Campi 213/A, I-41125 Modena, Italy

[3] Departiment of Physical, Informatics and Mathematical Sciences, Università di Modena e Reggio Emilia, Via Campi 213/A, I-41125 Modena, Italy

[4] Korea Advanced Institute of Science and Technology, Daejeon 305-338, Korea

[5] Laboratory of Bio-Inspired and Graphene Nanomechanics, Department of Civil, Environmental and Mechanical Engineering, University of Trento, via Mesiano 77, I-38123 Trento, Italy,

[6] School of Engineering and Materials Science, Queen Mary University of London, Mile End Road, E1 4NS London, UK

*Corresponding author: nicola.pugno@unitn.it

Morphological description of bare polycrystalline Ni and CVD grown graphene on polycrystalline Ni

The existence of flat areas and rough or stepped regions on CVD grown graphene is highlighted applying a local derivative operator (Gwyddion 2.38 open software, http://gwyddion.net/) to the raw topography data (Figure S1a). In the Figure S1, we present this procedure applied to Figure 1c of the manuscript. The procedure has been started from topography image (figure S1a). Then the results of the local derivative operator are shown in Figure S1b. Colour scale represents the local surface slope so that flat regions appear uniform and darker respect to steps and edges. From this analysis, it is evident that flat and uniform graphene regions (that we will refer to as graphene grain in the manuscript) are surrounded and separated by extended rough regions (graphene interface boundary IB in the manuscript). Graphene grains are characterised by a uniform and small slope

(brown regions) and because of their shape and size seems matching a single Ni grain. A statistical analysis reveals that graphene grain possess a typical lateral dimension between 500 and 1000 nm. The superposition over the local slope image (panel b) of the friction mask representing areas characterized by high friction values clearly shows that graphene grain possesses higher friction respect to graphene interfacial grain boundaries (IB).
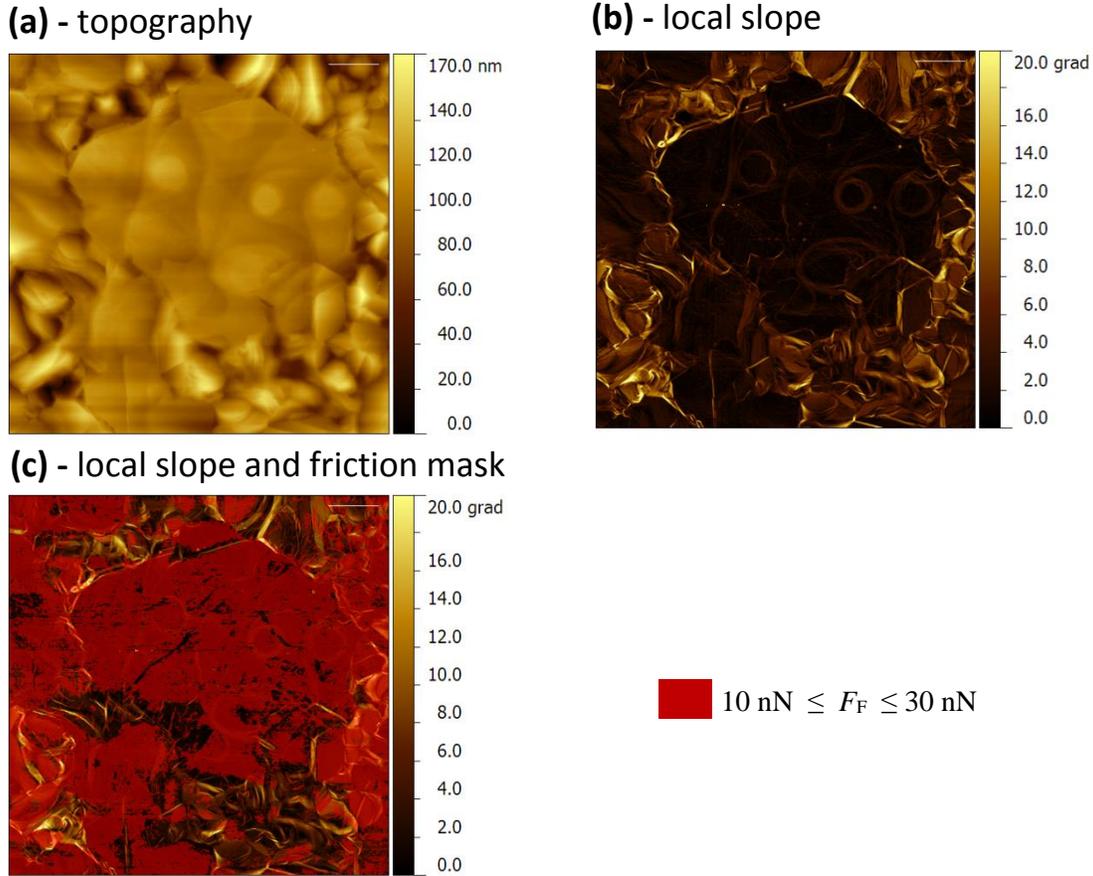
Figure S1: Procedure for the determination of substrate topography and related friction force signals. **(a)** Topography AFM image of a 15x15 μm^2 graphene region measured in contact mode. **(b)** Local derivative operator applied directly to the raw topography data. Color scale represents the local surface slope so that flat regions appear uniform and darker with respect to steps and edges. **(c)** Superposition over the local slope image (panel b) of a friction mask where red regions represent areas characterized by friction values between 10 and 30 nN.
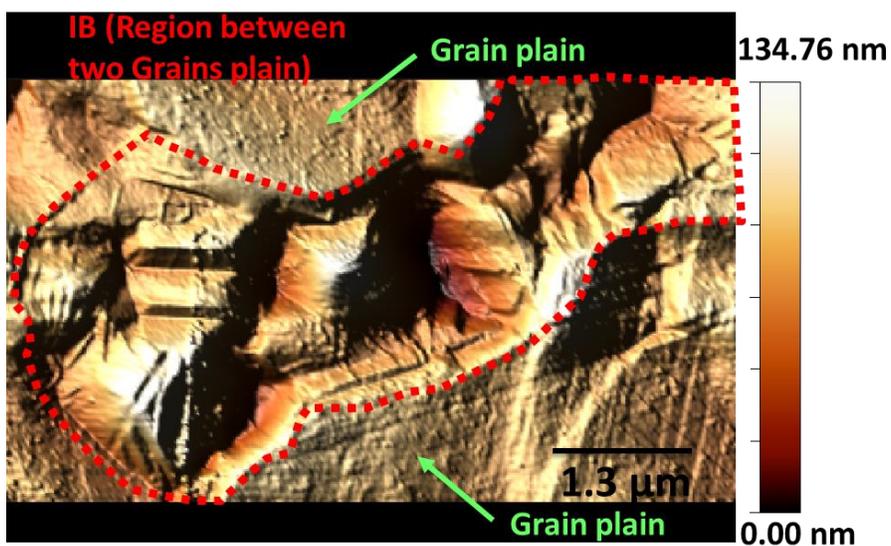
Figure S2: Intermittent contact mode, high resolution (steps/line 1024), 3D topographic image (6.5 x 3.8 µm²) of Gr/Ni-P sample. Green colour arrows are showing region of graphene covered grain plains of polycrystalline Ni. Within grains a region we refer to as Ni interface boundary (IB) is highlighted by the red colour dashed line. This region is separated by Ni grain and is highly disordered relatively to the flat surface of the grain plain. It comprises of a lump of carbon layers equivalent or higher than grain altitude (brightest colour as confirmed by scale bar). The width of IB region varies from 1 µm to 2.5 µm that include irregular carbon steps, plateaus and other irregular structures.
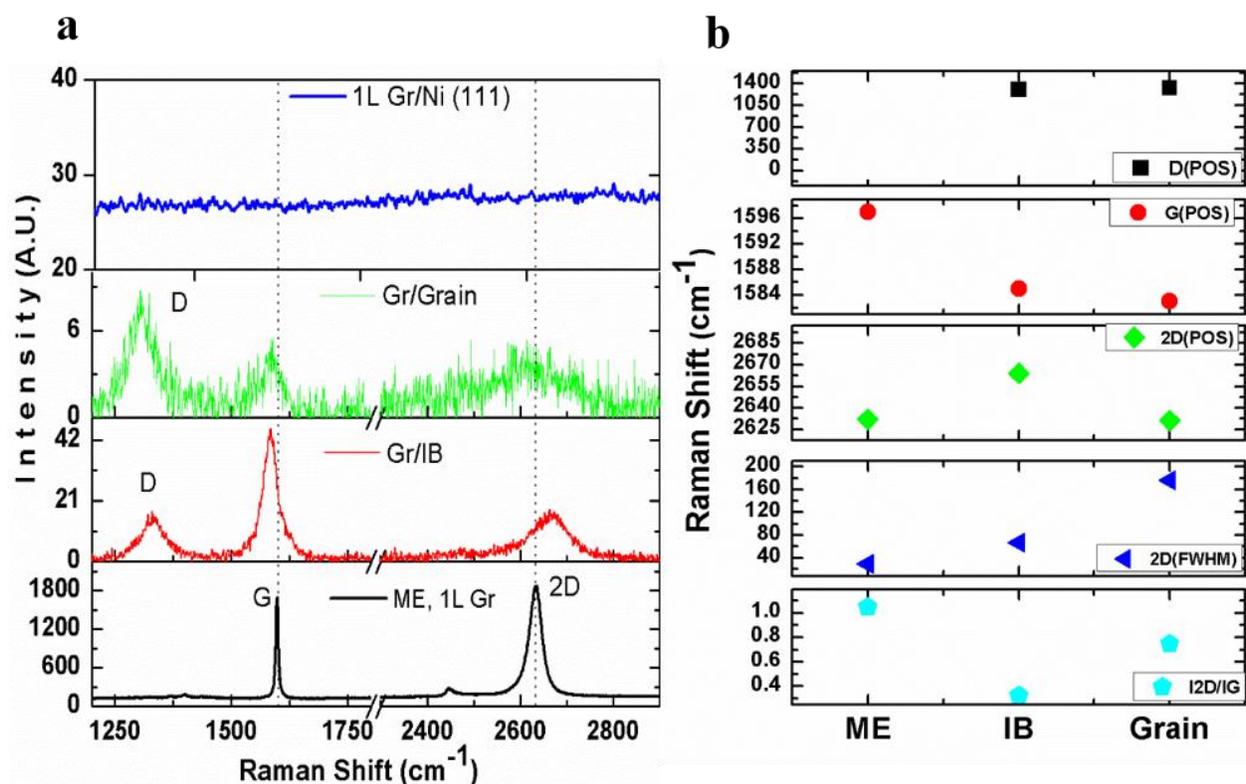
Figure S3: Raman spectra for evaluation of thickness of graphene layers over Gr/Ni-P along with reference, 1L Gr/SiO₂ and 1L Ni (111). (a) Raman Spectra of 1L graphene on Ni crystal, FLG on region of grain and interfacial boundaries (IB) and mechanically exfoliated 1L graphene on Silica. Graphene on silica shows relatively sharp peaks of G (~ 1597 cm⁻¹) and 2D (~ 2633 cm⁻¹) with no disorder induced peak (D). Spectra from 1L graphene over Ni crystal show suppression of all defined peaks. FLG shows presence of D, G and 2D peaks at ~ 1333 cm⁻¹, ~ 1587 cm⁻¹ and ~ 2667 cm⁻¹ respectively. The 2D peak is relatively suppressed at grain region with respect to interfacial boundaries. Vertical dashed line reveals shifting of peak positions (G and 2D) in CVD produced graphene with respect to mechanically exfoliated (ME) 1L graphene. **(b)** Quantitative values of peak position (POS) of D, G and 2D respectively from panel (a) with ratio of intensities between 2D and G peak (I2D/IG) and FWHM (full width of half maximum) using Lorentzian fitting.

Figure S3 shows μ-Raman spectra carried out at 1L graphene on Ni crystal (Ni (111)), silica substrate and FLG on grain and IB over polycrystalline Ni. Raman spectra for mechanically exfoliated 1L graphene on silica and CVD produced 1L graphene on Ni crystal are two extreme examples of graphene strain that influence the phononic vibration of carbon atoms. We observed total suppression of Raman shift peaks for 1L graphene on Ni crystal. For 1L graphene on silica, Raman shift peaks like G (~ 1597 cm^{-1}) and 2D (~ 2633 cm^{-1}) are clearly visible with no disorder induced peak (D). Raman spectrum for Gr/Ni-P lies in these two extreme cases, since it is influenced from Ni substrate, therefore, base line correction has been performed to eliminate background influence. The Raman shift of D, G and 2D peaks are observed at ~ 1333 cm^{-1}, ~ 1587 cm^{-1} and ~ 2667 cm^{-1} respectively. These wave numbers are relatively deviated from the spectra obtained from ME graphene used as a reference (Figure S3(b)). Multilayer graphene flakes formed on polycrystalline Ni films are usually stacked with deviations from the Bernal stacking type and show misorientation among the carbon layers[1]. Further, the doping (p-type) due to Ni metal for producing strain cannot be neglected[2]. The suppression of 2D peaks at the grain regions relative to IB has been observed. The peak of vibrational G band is attributed to the bond stretching of all pairs of sp2 atoms in both rings and chains form. However, suppression of 2D peak is associated with stronger chemical interaction, i.e. hybridization of the metal d-band with graphene π-states[2]. For one layer graphene on Ni (111), the chemical interaction between graphene and Ni leads to a large energy difference in the p_z orbital of graphene and a loss of the resonance conditions for Raman[2]. Consequently, no Raman signal for graphene on Ni (111) is observed under similar instrumental set-up ($\lambda = 632.8$ nm). In such situation, it is complex to calculate quantitative values of graphene thickness over Ni substrate. Nevertheless, qualitative estimation of graphene thickness and the presence of sp2 bonded carbon layers is feasible using intensity ratio I2D/IG. From Figure S3(b), the intensity ratio of 2D/G confirms that IB has higher accumulation of carbon layers than grain region; therefore the lateral force F_L contrasts (as describe in main text) obtained above arise from difference in thickness distribution of carbon layers and not from heterogeneity of the system.

In order to validate our argument for the suppression of the Raman 2D peak on Ni substrate, we performed Raman map of CVD produced graphene on Ni and transferred over silica (Gr/Si-T) through wet chemical procedure[3]. The optical image is shown in Figure S4(a): Raman probed spots (~1μm in diameter step) are labelled from A1 to E5. Its topographic image (rotated AFM image Figure S4(b)) reveals that brighter optical contrast has higher altitude (Z-direction) which can

originate from IB as discussed above. Raman map in such realm has scarce monolayer graphene (only at location "D4 with $I2D/IG \geq 1$") available (Figures S4(c) and S4(d)). The IB has a range of 4-7 (higher altitude region) and grain of 2-4 carbon layers under laser probe size of ~1 μm. Throughout investigation of Raman map no such suppression of 2D peaks has been observed relative to G and D peaks unlike Gr/Ni-P.
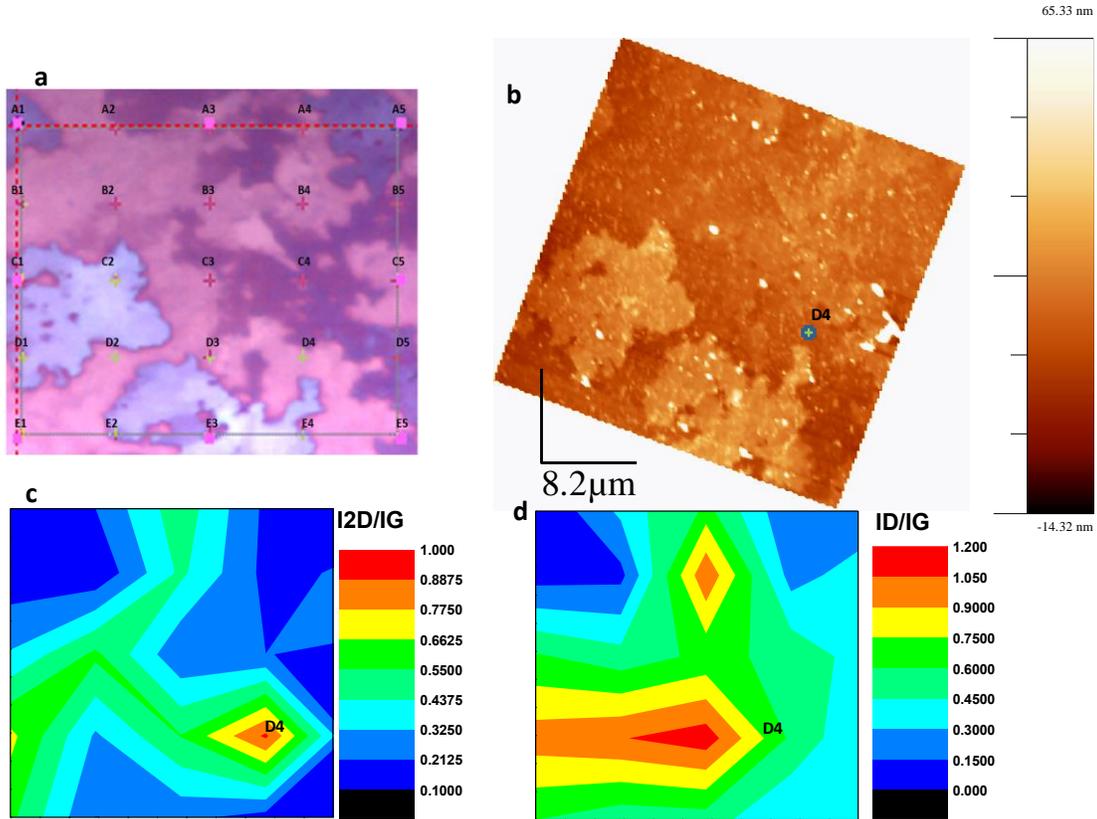
Figure S4: Raman mapping of CVD produced graphene on polycrystalline Ni and transferred to SiO$_2$. **(a)** Optical image of CVD produced FLG on Ni and transferred over silica substrate (Gr/Si-T). The red colour dashed rectangle corresponds to the area on which programmed Raman map has been carried out ($\approx$ 20 x 20 μm^2). The alphanumeric characters (A1 to E5) identify the Raman probe positions. **(b)** Tapping mode (flattened, height channel), the same region has been relocated in AFM apparatus. The topographic image has been aligned vertically for better comparison with optical image of panel (a). **(c)** Intensity ratio of Raman peak (2D/G) corresponding to position D4. **(d)** Intensity ratio of Raman peak (D/G). Position D4 shows 1L graphene (confirm from panel (c)) and its appearance in optical image (pink colour in panel (a) and AFM topography in panel (b)). Note that the resolution of panel (c) and (d) is not equivalent to panel (b) since distance between each Raman probed spot is 4 μm.

Finite element (FEM) simulations
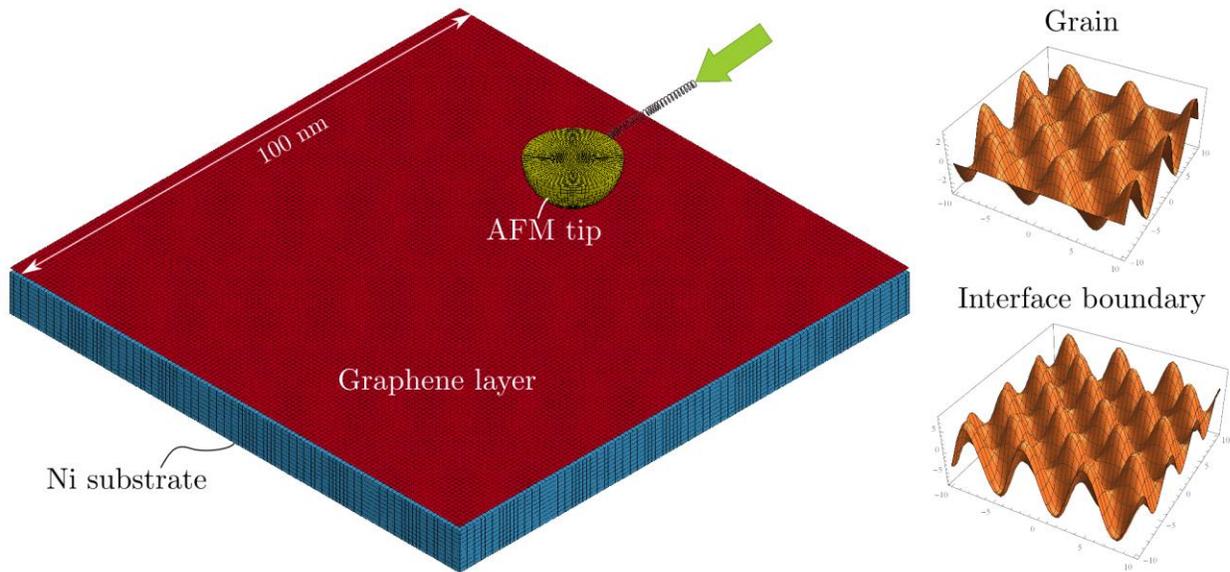
Figure S5: FEM simulations setup. The sliding tip is subjected to a constant imposed velocity which is applied on an auxiliary node linked to the hemisphere with a horizontal spring: this scheme allows to easily compute the friction force signal as the force acting in the spring during the sliding motion. The normal force is applied directly on the tip. The overall tip sliding displacement is of 50 nm, starting and terminating 25 nm far from the edges, which are fully clamped at the area edges. The substrate is also fixed at the base, blocking the vertical motion. The roughness of the substrate is translated in an equivalent sinusoidal surface in both the in-plane directions. The parameters defining the surface differ between grain and interfacial boundaries according to the experimental measured average roughness R_a (portions of the resulting profiles of 10x10 nm are depicted in the figure).

References

1. Zhang, Y.; Gao, T.; Xie, S.; Dai, B.; Fu, L.; Gao, Y.; Chen, Y.; Liu, M.; Liu, Z., Different growth behaviors of ambient pressure chemical vapor deposition graphene on Ni(111) and Ni films: A scanning tunneling microscopy study. *Nano Research* **2012,** *5* (6), 402-411.

2. Dahal, A.; Batzill, M., Graphene-nickel interfaces: a review. *Nanoscale* **2014,** *6* (5), 2548-62.

3. Li, X.; Zhu, Y.; Cai, W.; Borysiak, M.; Han, B.; Chen, D.; Piner, R. D.; Colombo, L.; Ruoff, R. S., Transfer of Large-Area Graphene Films for High-Performance Transparent Conductive Electrodes. *Nano Letters* **2009,** *9* (12), 4359-4363.